Structural, elastic and electronic properties of MgB_2C_2 under pressure from first-principles calculations

Lili Liu[1,2,*], Miao Wang[1], Lei Hu[3], Yufeng Wen[4,†], Youchang Jiang[1]

[1] *Department of Physics, Chongqing Three Gorges University, 404100, China*

[2] *Institute for Structure and Function, Chongqing University, 401331, China*

[3] *School of Environmental and Chemical Engineering, Chongqing Three Gorges University, 404100, China*

[4] *School of Mathematical Sciences and Physics, Jinggangshan University, 343009, China*

Abstract: First principles calculations by using of projected augmented plane-wave method have been performed to investigate the structural, elastic and electronic properties of MgB_2C_2 under different pressures. The results indicate that the ternary compound of MgB_2C_2 remains mechanically stable under pressure ranging from 0 to 50 GPa. Elastic analysis is performed and it is found that MgB_2C_2 always shows obvious intrinsic brittleness under pressure, although an increasing trend of the ductility both from B_H/G_H and ν_H with increasing pressure. (100), (010) and $(1\bar{1}0)$ planes show strong anisotropy and the degree of anisotropy decreases with increasing pressure, in the meantime, it is interesting to find that the degree of anisotropy is reduced in order of planes $(1\bar{1}0) \rightarrow (100) \rightarrow (010)$ under the same pressure.

Keywords: MgB_2C_2; elastic properties; high pressure; first-principles calculations

1. Introduction

In 2001, the discovery of superconductivity in MgB_2 at 36 K [1] triggered an enormous interest in detecting superconductivity in related compounds. The technical performance of the MgB_2 superconductor can be improved through doping [2]. For example, doping carbon into MgB_2 can drastically increase the resistivity and upper critical field at the cost of decreasing the transition temperature T_c [3]. As reported in the literature [4–7], mainly six binary compounds (MgB_2, MgB_4, MgB_7, MgC_2, Mg_2C_3 and B_4C) and one ternary compound (MgB_2C_2) exist in the Mg-B-C phase system. Of these, MgB_2C_2, the first borocarbide of magnesium, belongs to the orthorhombic system, Cmca-D_{2h}^{18} space group (No. 64), and figure 1 presents its crystal

*E-mail: liulili0612@163.com

†E-mail: jgsuwyf@sina.com

structure. There are eight formula units (40 atoms) and eight symmetrically independent in the unit cell. The structure of MgB_2C_2 is similar to graphite. The main distinction between graphite and MgB_2C_2 is that the borocarbide hexagonal layer in MgB_2C_2 is slightly puckered with a maximum deviation of 20 pm from the optimized plane. The charge of puckered $^2_\infty[BC]^-$ layers is counterbalanced by the Mg^{2+} cations. Each Mg cation is coordinated by six boron atoms and six carbon atoms, forming a slightly distorted hexagonal prism. Structurally compared with graphite, MgB_2C_2 has a larger average layer distance, which may be explained by the less effective shielding of the negative charge owing to the reduced number of cations between the layers.

Experimentally, Wörle reported the high-pressure modifications of MgB_2C_2 using the high resolution transmission electron microscopy (HRTEM) image, the electron energy loss spectrum (EELS), and energy-dispersive X-ray spectrum (EDXS) [8]. Susner et al. used high-pressure, high-temperature apparatus at 1500-1700 ^oC and 10 MPa to synthesize large-grained MgB_2 and MgB_2C_2 [9]. Theoretically, Ravindran et al. investigated the electronic ground state properties of MgB_4, MgB_2C_2, and LiBC using the TB-LMTO method of Andersen [10]. Harima calculated the energy band structures of MgB_2, LiBC, and MgB_2C_2 using the LDA and first-principles full potential linearized augmented plane wave (FPLAPW) method [11]. Verma calculated the electronic band structure of the compound MgB_2C_2 and its hole-doped derivatives $Mg_{0.5}Li_{0.5}B_2C_2$, $Mg_{0.5}Na_{0.5}B_2C_2$, $Mg_{0.9}Na_{0.1}B_2C_2$ and $Mg_{0.5}K_{0.5}B_2C_2$ using the FPLAPW calculations [12]. Spanò found that hole-doped MgB_2C_2 has a large electron-phonon coupling constant according to the density functional perturbation theory [13]. Lebègue studied the chemical bonding of MgB_2C_2 via the Projector Augmented Plane wave method together with the crystal orbital overlap population (COOP) technique [14]. Obviously, all these results predominantly concentrate on the electronic and band structure.

The elastic properties are closely linked with many fundamental phenomena such as equation of state (EOS), interatomic bonding and phonon spectra, melting point, specific heat, thermal expansion, Debye temperature and Grüneisen parameter. To our knowledge, the elastic constants of MgB_2C_2 as a function of temperature were studied via the first-principles phonon [15], but the related properties are never explored. Further, elastic constants under high pressure are crucial for understanding strength, mechanical stability and phase transition of materials. Therefore, in the present work, the elastic constants and some related properties of MgB_2C_2 in the pressure range of 0-50 GPa are studied by using the first-principles calculations, to provide new insights on structural, elastic anisotropy, acoustic and electronic properties under pressure. We hope that this work promotes researches on the pressure dependence of elastic and electronic properties for MgB_2-related materials. The rest of the paper is organized as follow. The computational details are described in Section 2. Some results and discussion are presented in Section 3. Finally, a brief summary and conclusions are given in Section 4.

2. Computational details

Herein, Vienna ab-initio simulation package (VASP) code based on the density functional theory (DFT) was conducted [16–18]. Perdew-Burke-Ernzerhof (PBE) functional parameterization was implemented within the generalized gradient approximation (GGA) [19, 20] as well as projector augmented wave (PAW) method [21, 22]. Appropriate pseudopotentials for Mg $2p^6 3s^2$, B $2s^2 2p^1$ and C $2s^2 2p^2$ configurations as valence electrons were selected to achieve the higher convergence rate. A plane wave cut-off energy value of 600 eV was used and the Monkhorst-Pack scheme with 4×4×5 grids was adopted [23] to calculate the lattice and elastic parameters under different pressures within the atomic forces became less than 0.01 eV/Å to ensure the accuracy of the calculations. The stress-strain relationship method was used to determine the elastic constants. Because of the large size of MgB_2C_2, full relaxation was taken into account of all the calculations.

3. Results and discussion

3.1. Structural properties

Tables 1 and 2 list the calculated lattice parameters of MgB_2C_2 at 0 GPa together with the experimental [24] and theoretical [25] results. One can find that the lattice parameters we calculated do not differ from the experimental values by more than 0.23% and the difference between our result and Spanò's reported data is less than 1.53%. Besides, the corrugation of the borocarbide planes is 0.207 Å, which agree well with the experimental data 0.207 Å and Spanò's reported value 0.194 Å. Therefore, our calculations are correct. To study the influence of external pressure on the crystal structure of MgB_2C_2, figure 2 shows the normalized lattice parameters a/a_0, b/b_0, c/c_0 and the normalized volume V/V_0 under different pressures, where a_0, b_0, c_0 and V_0 refer to the equilibrium lattice parameters and the volume at 0 GPa, respectively. Obviously, the lattice parameters and volume automatically decrease with pressure. The axial and volume compression can be accurately described by fitting the data under different pressures with a second-order polynomial

$$\begin{aligned} a/a_0 &= 0.99979 - 1.22 \times 10^{-3} \times P + 7.89 \times 10^{-6} \times P^2 \\ b/b_0 &= 0.99982 - 1.23 \times 10^{-3} \times P + 9.08 \times 10^{-6} \times P^2 \\ c/c_0 &= 0.99874 - 3.86 \times 10^{-3} \times P + 1.93 \times 10^{-5} \times P^2 \\ V/V_0 &= 0.99814 - 6.17 \times 10^{-3} \times P + 3.91 \times 10^{-5} \times P^2 \end{aligned} \tag{1}$$

where the Adj. R^2 value is the correlation coefficient. The Adj. R^2 values are 0.999, 0.999, 0.998 and 0.998 for a/a_0, b/b_0, c/c_0, and V/V_0, respectively. All values are close to 1, revealing that the fit is a good one. The reduction in atomic distance and the increase in inter-atomic repulsive force renders compression difficult under pressure. Figure 2 shows that the compression capabilities of different axes are different, and the compression

capability along the c axis is significantly bigger than that along the a or b axis.

3.2. Pressure dependent elastic properties

Elastic constants are important properties of solids that are useful for understanding mechanical properties and structural stability. Table 3 presents the elastic constants of MgB_2C_2 under different pressures. However, no other experimental and theoretical values are available. All elastic constants, excluding C_{33}, continuously increase with the pressure. The orthorhombic structure of MgB_2C_2 under different pressures will become mechanically stable when its elastic constants satisfy the following inequalities [26]:

$$\begin{gathered}\widetilde{C}_{11}+\widetilde{C}_{22}-2\widetilde{C}_{12}>0,\quad \widetilde{C}_{11}+\widetilde{C}_{33}-2\widetilde{C}_{13}>0,\quad \widetilde{C}_{22}+\widetilde{C}_{33}-2\widetilde{C}_{23}>0\\ \widetilde{C}_{11}>0,\quad \widetilde{C}_{22}>0,\quad \widetilde{C}_{33}>0,\quad \widetilde{C}_{44}>0,\quad \widetilde{C}_{55}>0,\quad \widetilde{C}_{66}>0\\ \widetilde{C}_{11}+\widetilde{C}_{22}+\widetilde{C}_{33}+2\widetilde{C}_{12}+2\widetilde{C}_{13}+2\widetilde{C}_{23}>0\end{gathered} \tag{2}$$

where $\widetilde{C}_{\alpha}=C_{\alpha\alpha}-P(\alpha=1\sim 6)$, $\widetilde{C}_{12}=C_{12}+P$, $\widetilde{C}_{13}=C_{13}+P$, and $\widetilde{C}_{23}=C_{23}+P$. Through calculations, it is not difficult to find that the orthorhombic structure of MgB_2C_2 is mechanically stable in the pressure range of 0-50 GPa.

With the knowledge of single-crystal elastic constants, the polycrystalline elastic moduli are estimated by several methods, including Voigt's, Reuss's and Hill's approximation [27–29]. For the orthorhombic phase, the Voigt's and Reuss's moduli are estimated by [30]

$$\begin{gathered}B_V=\frac{1}{9}\Big[C_{11}+C_{12}+C_{33}+2(C_{11}+C_{13}+C_{23})\Big]\\ B_R=\frac{1}{S_{11}+S_{22}+S_{33}}+2(S_{12}+S_{13}+S_{23})\\ G_V=\frac{1}{15}\Big[C_{11}+C_{22}+C_{33}+3(C_{44}+C_{55}+C_{66})-(C_{12}+C_{13}+C_{23})\Big]\\ G_R=\frac{15}{4(S_{11}+S_{22}+S_{33})-4(S_{12}+S_{13}+S_{23})+3(S_{44}+S_{55}+S_{66})}\end{gathered} \tag{3}$$

Let S_{ij} be the elastic compliance constants

$$\begin{gathered}S_{11}=\frac{C_{22}C_{33}-C_{23}^2}{\Delta},\quad S_{22}=\frac{C_{11}C_{33}-C_{13}^2}{\Delta},\quad S_{33}=\frac{C_{11}C_{22}-C_{12}^2}{\Delta}\\ S_{12}=\frac{C_{13}C_{23}-C_{12}C_{23}}{\Delta},\quad S_{13}=\frac{C_{11}C_{23}-C_{13}C_{22}}{\Delta},\quad S_{23}=\frac{C_{12}C_{23}-C_{11}C_{23}}{\Delta}\\ S_{ii}=\frac{1}{C_{ii}}(i=4,5,6),\quad \Delta=C_{13}(C_{12}C_{23}-C_{13}C_{22})+C_{23}(C_{12}C_{13}-C_{23}C_{11})+C_{33}(C_{11}C_{22}-C_{12}^2)\end{gathered} \tag{4}$$

and Hill's bulk (B_H) and shear (G_H) moduli by [27]

$$B_H=\frac{B_V+B_R}{2},\qquad G_H=\frac{G_V+G_R}{2} \tag{5}$$

Hill's Young's modulus (E_H) and Hill's Poisson's ratio (ν_H) are further written by [27]

$$E_H = \frac{9B_H G_H}{3B_H + G_H}, \quad \nu_H = \frac{3B_H - 2G_H}{6B_H + 2G_H} \tag{6}$$

Figure 3(a) shows B_H, G_H and E_H of MgB_2C_2 as a function of pressure. It is obvious that B_H, G_H and E_H increase continuously with pressure and E_H exhibits the biggest changes. These results imply that the covalent bonding property of MgB_2C_2 becomes more dominant with increasing pressure. Figure 3(b) shows the B_H/G_H and ν_H under different pressures. Both B_H/G_H and ν_H values can be employed to evaluate the ductile/brittle behaviour of a material. As suggested by Pugh [31], the materials with a higher B_H/G_H ratio than 1.75 exhibit ductile behaviour, otherwise behaves in a brittle manner. All values of B_H/G_H are less than 1.75 here, thus, MgB_2C_2 is brittle within 50 GPa. The B_H/G_H ratio increases as pressure increases, indicating that its brittleness decreases with increasing pressure. In contrast, ν_H is larger or less than 1/3 for ductile and brittle materials, respectively [32]. Therefore, the conclusion obtained from Poisson's ratio is identical to that obtained from the B_H/G_H ratio.

3.3. Pressure dependent elastic anisotropy

Crystals are seldom elastically isotropic and their anisotropy is crucial in engineering science because it can potentially induce microcracks in materials [33]. The shear anisotropy factor of MgB_2C_2 along the {100} plane between $< 011 >$ and $< 010 >$ directions is [34]

$$A^{\{100\}} = \frac{4C_{44}}{C_{11} + C_{33} - 2C_{13}} \tag{7}$$

For the {010} plane between $< 101 >$ and $< 001 >$ directions, it can be expressed as [34]

$$A^{\{010\}} = \frac{4C_{55}}{C_{22} + C_{33} - 2C_{23}} \tag{8}$$

and for the {001} plane between $< 110 >$ and $< 010 >$ directions, it can be written as [34]

$$A^{\{001\}} = \frac{4C_{66}}{C_{11} + C_{22} - 2C_{12}} \tag{9}$$

The deviation of $A^{\{100\}}$, $A^{\{010\}}$ and $A^{\{001\}}$ from one represents the degree of its shear anisotropy. Figure 4(a) presents the anisotropic factors of MgB_2C_2 under different pressures. Moreover, $A^{\{100\}}$ and $A^{\{010\}}$ are much less than 1 and increase by 56.1% and 55.7%, respectively, whereas $A^{\{001\}}$ decreases by approximately 23.5% and $A^{\{001\}}$ has the biggest values compared with $A^{\{100\}}$ and $A^{\{010\}}$ over the whole pressure range investigated. These results demonstrate that the shear anisotropy of the {100} and {010} planes decrease and that of the {001} plane shows an opposite trend with increasing pressure. Furthermore, the shear plane {001} exhibits more isotropic properties than the {100} and {010} shear planes over the entire pressure range.

In polycrystals, the percentage anisotropy in bulk (A^B) and shear (A^G) moduli are [35]

$$A^B = \frac{B_V - B_R}{B_V + B_R}, \qquad A^G = \frac{G_V - G_R}{G_V + G_R} \tag{10}$$

The universal elastic anisotropy parameter A^U is defined as [36]

$$A^U = \frac{B_V}{B_R} + 5\frac{G_V}{G_R} - 6 \tag{11}$$

Furthermore, the log-Euclidean anisotropy parameter is defined as [37]

$$A^L = \sqrt{\Big[\ln(\frac{B_V}{B_R})\Big]^2 + 5\Big[\ln(\frac{G_V}{G_R})\Big]^2} \tag{12}$$

For these four anisotropic indexes, positive non-zero values correspond to the degree of anisotropy. Figure 4 presents the relationship between the anisotropic indexes and pressure up to 50 GPa. A^B increases slightly and A^G decreases sharply with increasing pressure. In addition, the values of A^G are greater than those of A^B under the same pressure. This indicates that the anisotropy in compressibility is significantly weaker than that in shear. As the pressure increases, both A^U and A^L have the same change trend with A^G.

With the knowledge of compliance constants, Young's modulus (E) and shear modulus (G) can be calculated as a function of orientation. For the orthorhombic system, the directional dependence in the (001) plane are [38]:

$$\begin{aligned} E^{-1} &= S_{11}\cos^4\alpha + S_{22}\sin^4\alpha + 2S_{12}\sin^2\alpha\cos^2\alpha + S_{66}\sin^2\alpha\cos^2\alpha \\ G^{-1} &= S_{55} + (S_{44} - S_{55})\sin^2\alpha \end{aligned} \tag{13}$$

and in the (100) plane [38]:

$$\begin{aligned} E^{-1} &= S_{22}\sin^4\alpha + S_{33}\cos^4\alpha + \frac{1}{4}(2S_{23} + S_{44})\sin^2 2\alpha \\ G^{-1} &= S_{55} + (S_{66} - S_{55})\sin^2\alpha \end{aligned} \tag{14}$$

and in the (010) plane [38]:

$$\begin{aligned} E^{-1} &= S_{11}\sin^4\alpha + S_{33}\cos^4\alpha + \frac{1}{4}(2S_{13} + S_{55})\sin^2 2\alpha \\ G^{-1} &= S_{44} + (S_{66} - S_{44})\sin^2\alpha \end{aligned} \tag{15}$$

and in the $(1\bar{1}0)$ plane [38]:

$$\begin{aligned} E^{-1} &= \frac{\sin^4\alpha}{(a^2+b^2)^2}\Big[a^4S_{11} + b^4S_{12} + a^2b^2(2S_{12} + S_{66})\Big] + S_{33}\cos^4\alpha + \frac{\sin^2\alpha\cos^2\alpha}{a^2+b^2}\Big[a^2(2S_{13} + S_{55}) + b^2(2S_{23} + S_{44})\Big] \\ G^{-1} &= \frac{\sin^2\alpha}{(a^2+b^2)^2}\Big[a^2b^2(4S_{11} + 4S_{22} - 8S_{12}) + (b^2 - a^2)^2S_{66}\Big] + \frac{\cos^2\alpha}{a^2+b^2}(a^2S_{44} + b^2S_{55}) \end{aligned} \tag{16}$$

where α is made with the [001] direction.

Variations of Young's modulus and shear modulus with orientation in the (100), (010), (001) and $(1\bar{1}0)$ planes under different pressures are displayed in figure 5 and figure 6, respectively. At 0 GPa, the shapes of Young's modulus and shear modulus in the (001) plane are nearly round, implying that they are nearly isotropic. The finding agree well with the result obtained from the above shear anisotropy factor $A^{\{001\}}$. The Young's modulus and shear modulus in the (100), (010) and $(1\bar{1}0)$ planes under different pressures show strong anisotropy and their degree of anisotropy decrease with increasing pressure. Taking the shear modulus as an example, the minimum and maximum in the (100) plane correspond to 32.68 and 229.51 GPa for 0 GPa, 64.17 and 258.21 GPa for 30 GPa, as well as 79.35 and 270.46 GPa for 60 GPa; its minimum and maximum in the (010) plane correspond to 38.16 and 229.52 GPa for 0 GPa, 75.08 and 258.21 GPa for 30 GPa, as well as 101.73 and 270.46 GPa for 50 GPa; and its minimum and maximum in the $(1\bar{1}0)$ plane correspond to 35.60 and 252.54 GPa for 0 GPa, 69.98 and 325.55 GPa for 30 GPa, as well as 90.71 and 365.54 GPa for 50 GPa. The ratios of the maximum and the corresponding minimum in the (100) ((010), $(1\bar{1}0)$) are 7.02 (6.01, 7.09), 4.02 (3.44, 4.65) and 3.41 (2.66, 4.03) for 0 GPa, 30 GPa and 50 GPa, respectively. Obviously, the ratios of the maximum and the corresponding minimum decrease with pressure. Besides, it is interesting to find that the degree of anisotropy is reduced in order of planes $(1\bar{1}0) \rightarrow (100) \rightarrow (010)$ under different pressures.

3.4. Pressure dependent acoustic and related properties

Debye temperature (Θ_D) is an important physical quantity of solids. It often occurs in equation describing properties which arises from lattice vibrations. One way to calculate the Θ_D is as follows [39]:

$$\Theta_D = \frac{h}{k_B}\left[\frac{3n}{4\pi}\left(\frac{N_A\rho}{M}\right)\right]^{\frac{1}{3}} V_M \tag{17}$$

where h/k_B are the usual meanings of quantum mechanics, N_A is the Avogadro's number, M is the molecular weight and n is the number of atoms in the unit cell. The expression for the mean acoustic velocity V_m is [39]

$$V_M = \left[\frac{1}{3}\left(\frac{1}{V_L^3} + \frac{2}{V_T^3}\right)\right]^{-\frac{1}{3}} \tag{18}$$

where V_L and V_T are the longitudinal and transverse elastic wave velocities, respectively. Using the Navier's equation [40], they are

$$V_L = \sqrt{\frac{3B_H+4G_H}{3\rho}}, \quad V_T = \sqrt{\frac{G_H}{\rho}} \tag{19}$$

Table 4 lists the calculated ρ and various acoustic velocities under different pressures. Unfortunately, no experimental and theoretical values are available for comparison. It can be seen from Table 4 that all the calculated values increase with increasing pressure. Furthermore, the Debye temperature represents interatomic force, hence, higher Debye temperatures represent stronger bonds. The results obtained from the Debye temperature are consistent with the behavior from the Young's modulus results described above.

In anisotropic single-crystals, the propagation of elastic waves is governed by the famous Christoffel's equation [41]. The elements of the Christoffel determinants are given on the basis of mass density and elastic constants

$$(\sum_{k=1}^{3}\sum_{m=1}^{3} C_{ikjm}l_k l_m - \rho v^2\delta_{ij})u_j = 0 \tag{20}$$

where C_{ikjm} is the stiffness matrix, l_k and l_m are the directional cosines, ρ is the density, v is the sound velocity and u_j represents the displacement vector. The wave velocities along the different propagating directions can be formulated by solving the eigenvalues of the following eigenfunction:

$$\begin{bmatrix} \alpha-\rho v^2 & \delta & \zeta \\ \delta & \beta-\rho v^2 & \varepsilon \\ \zeta & \varepsilon & \gamma-\rho v^2 \end{bmatrix}\begin{bmatrix} u_1 \\ u_2 \\ u_3 \end{bmatrix} = 0 \tag{21}$$

with

$$\begin{cases} \alpha = C_{11}l_1^2 + C_{66}l_2^2 + C_{55}l_3^2 \\ \beta = C_{66}l_1^2 + C_{22}l_2^2 + C_{44}l_3^2 \\ \gamma = C_{55}l_1^2 + C_{44}l_2^2 + C_{33}l_3^2 \\ \sigma = (C_{12}+C_{66})l_1l_2 \\ \varepsilon = (C_{23}+C_{44})l_2l_3 \\ \zeta = (C_{13}+C_{55})l_3l_1 \end{cases} \tag{22}$$

The longitudinal (v_l), first transverse (v_{t1}) and second transverse (v_{t2}) wave velocities for MgB_2C_2 along the six principal axes containing [100], [010], [001], [110], [101] and [011] directions are obtained as follows

$$\begin{gathered} [100]v_l = \sqrt{\tfrac{C_{11}}{\rho}},\ \ [010]v_l = \sqrt{\tfrac{C_{22}}{\rho}},\ \ [001]v_l = \sqrt{\tfrac{C_{33}}{\rho}} \\ [100]v_{t1} = [010]v_{t1} = \sqrt{\tfrac{C_{66}}{\rho}},\ \ [100]v_{t2} = [001]v_{t1} = \sqrt{\tfrac{C_{55}}{\rho}},\ \ [010]v_{t2} = [001]v_{t2} = \sqrt{\tfrac{C_{44}}{\rho}} \\ [110]v_l = \sqrt{\tfrac{C_{44}+C_{55}}{2\rho}},\ \ [110]v_{t1} = [110]v_{t2} = \sqrt{\tfrac{C_{11}+C_{22}+2C_{66}}{4\rho}} \\ [101]v_l = \sqrt{\tfrac{C_{44}+C_{66}}{2\rho}},\ \ [101]v_{t1} = [101]v_{t2} = \sqrt{\tfrac{C_{11}+C_{33}+2C_{55}}{4\rho}} \\ [011]v_l = \sqrt{\tfrac{C_{55}+C_{66}}{2\rho}},\ \ [011]v_{t1} = [011]v_{t2} = \sqrt{\tfrac{C_{22}+C_{33}+2C_{44}}{4\rho}} \end{gathered} \tag{23}$$

Table 4 presents the various acoustic velocities of MgB_2C_2 in the pressure range of 0-50 GPa. Generally, the elastic anisotropy of a crystalline material can be characterized by its acoustic velocity anisotropy. Two pure transverse modes exist along the [100], [010] and [001] directions, however, two degenerate transverse waves exist along the [110], [101] and [011] directions. Under different pressures, the longitudinal sound velocity satisfies the relation $[100]v_l > [010]v_l > [001]v_l > [101]v_l > [011]v_l > [110]v_l$.

Thermal conductivity is an intrinsic property of a material, which depends on the composition and temperature of the material. Several existing empirical methods can calculate the thermal conductivity of a material at a temperature higher than the Debye temperature: Clarke's model [42] and Cahill's model [43, 44]. When the temperature increases, the thermal conductivity decreases to a certain point called minimum thermal conductivity ($k_{\min}$). According to the Cahill's model [43, 44], $k_{\min}$ is estimated from the terms of v_l, v_{t1} and v_{t2} by

$$k_{\min} = \frac{k_B}{2.48}\left(\frac{n\rho N_A}{M}\right)^{\frac{2}{3}}(v_l + v_{t1} + v_{t2}) \tag{24}$$

Compared with Clarke's model, Cahill's model can more accurately quantify the anisotropy of thermal conductivity because it contains the three acoustic velocities (v_l, v_{t1} and v_{t2}). Table 6 lists the $k_{\min}$ and the thermal conductivity along the longitudinal and transverse acoustic branches (k_l, k_{t1} and k_{t2}) in the different propagation directions under different pressures, wherein, the calculated thermal conductivities exhibit anisotropic properties under different pressures owing to their anisotropic sound velocities, and $k_{\min}$ is reduced in the order of direction [110] → [010] → [100] → [101] → [011] → [001]. Moreover, $k_{\min}$ automatically increases with increasing pressure, which exhibits the same trend as that of the Debye temperature. The same change trend of the minimum thermal conductivity and the Debye temperature with pressure satisfy the Callaway-Debye theory [45].

3.5. Effect of pressure on electronic properties

Electronic structures are essential to understand the conducting, semiconducting, and insulating properties of materials. These properties are determined by electronic structures near the Fermi level (E_F). Figure 7 presents the calculated total and partial densities of states (DOSs) of MgB_2C_2 under different pressures. At zero pressure (0 GPa), an energy gap of 1.064 eV can be found in the total DOS near the E_F, showing that MgB_2C_2 is a semiconductor as reported in the literature [7, 15]. The gap's value agrees well with previous calculations [15]. All atoms contribute to the semiconductivity of the compound. According to figure 10(a), all DOS peaks at 30 GPa and 50 GPa have a tendency close to the E_F, that is, the valance bands shift to the high energy zone whereas the conduction bands move to the low energy zone. This tendency implies that the semiconductor band gap of MgB_2C_2 can narrow as the pressure increases from 0 to 50 GPa. Thus, its semiconductivity reduces with increasing pressure. Similar to that observed at 0 GPa, all atoms contribute to the semiconductivity observed at 50 GPa.

4. Conclusions

The structural, elastic, anisotropy, acoustic, thermal, and electronic properties of MgB_2C_2 under different

pressures have been investigated by using the first principles calculations. The lattice constants at 0 GPa agree well with the previous experimental and theoretical values. Both elastic and compliance constants of MgB_2C_2 under different pressures are further calculated, along with some related properties including bulk, shear and Young's moduli, Poisson's ratio, anisotropic factors, sound velocities, Debye temperature and minimum thermal conductivity. The compound is found to have mechanical stability and intrinsical brittle in the pressure range of 0-50 GPa, but its ductility increase with pressure. {001} plane is nearly isotropic at 0 GPa from shear anisotropy factor, Young's modulus and shear modulus. However, the Young's modulus and shear modulus in the (100), (010) and $(1\bar{1}0)$ planes under different pressures show strong anisotropy and their degree of anisotropy decrease with increasing pressure. Besides, it is interesting to find that the degree of anisotropy is reduced in order of planes $(1\bar{1}0) \rightarrow (100) \rightarrow (010)$ under different pressures. Further, it is found that the Debye temperature and the minimum thermal conductivity increase with increasing pressure.

Funding Information: The work is supported by the Science and Technology Research Program of Chongqing Municipal Education Commission (Grant No. KJQN201901217) and the Natural Science Foundation of China (51661013).

References

[1] J. Nagamatsu, N. Nakagawa, T. Muranaka, Y. Zenitani, J. Akimitsu, Nature, 410 (2001) 63.

[2] K. Vinod, N. Varghese, U. Syamaprasad, Supercond Sci Technol 20 (2007) R31.

[3] A. V. Pogrebnyakov, X. X. Xi, J. M. Redwing, V. Vaithyanathan, D. G. Schlom, A. Soukiassian, et al. Appl. Phys. Lett. 85 (2004) 2017.

[4] J. Z. Novak, Phys. Chem. (Muenchen, Ger.) 73 (1910) 513.

[5] A. A. Nayeb-Hashemi, J. B. Clark, B-Mg. Materials Park, OH: ASM International: 1988.

[6] H. Okamoto, J. Phase Equilib 13 (1992) 436.

[7] M. Worle, R. Nesper, J. Alloy Compd. 216 (1994) 75.

[8] M. Wörle, U. Fischbach, D. Widmer, F. Krumeich, R. Nesper, J. Evers, R. Stalder, P. Ulmer, Z. Anorg. Allg. Chem. 636 (2010) 2543.

[9] M. A. Susner, S. D. Bohnenstiehl, S. A. Dregia, M. D. Sumption, Y. Yang, J. J. Donovan, E. W. Collings, Appl. Phys. Lett. 104 (2014) 162603.

[10] P. Ravindran, P. Vajeeston, R. Vidya, A. Kjekshus, H. Fjellvåg, Phys. Rev. B 64 (2001) 224509.

[11] H. Harima, Physica C 378-381 (2002) 18.

[12] A. K. Verma, P. Modak, D. M. Gaitonde, R. S. Rao, B. K. Godwal, L. C. Gupta, Europhys. Lett. 63 (2003) 743.

[13] E. Spanò, M. Bernasconi, E. Kopnin, Phys. Rev. B 72 (2005) 014530.

[14] S. Lebègue, B. Arnaud, M. Alouani, Comput. Mater. Sci. 37 (2006) 220.

[15] A. Saengdeejing, Y. Wang, Z. K. Liu, Intermetallics, 18 (2010) 803.

[16] G. Kresse, J. Hafner, Phys. Rev. B 48 (1993) 3115.

[17] G. Kresse, J. Furthmller, Comput. Mater. Sci. 6 (1996) 15.

[18] G. Kresse, J. Furthmller, Phys. Rev. B 54 (1996) 11169.

[19] J. P. Perdew, K. Burke, M. Ernzerhof, Phys. Rev. Lett. 77 (1996) 3865.

[20] J. P. Perdew, K. Burke, M. Ernzerhof, Phys. Rev. Lett. 78 (1996) 1396.

[21] P. E. Blöchl, Phys. Rev. B 50 (1994) 17953.

[22] G. Kresse, D. Joubert, Phys. Rev. B 59 (1999) 1758.

[23] H. J. Monkhorst, J. D. Pack, Phys. Rev. B 13 (1976) 5188.

[24] M. Wörle, R. Nesper, J. Alloys Compd. 216 (1994) 75.

[25] E. Spanò, M. Bernasconi, Phys. Rev. B 72 (2005) 014530.

[26] G. V. Sin'ko, N. A. Smirnov, J. Phys.: Condens. Matter 14 (2002) 6989.

[27] R. Hill, Proc. Phys. Soc. A 65 (1952) 349.

[28] W. Voigt, Lehrbuch der kristallphysik, Leipzig, Taubner, 1928.

[29] A. Reuss, Z. Angew. Math. Mech. 9 (1929) 49.

[30] S. N. Li, X. Ju, C. B. Wan, Comput. Mater. Sci. 81 (2014) 378.

[31] S. F. Pugh, Philos. Mag. 45 (1954) 823.

[32] I. N. Frantsevich, F. F. Voronov, S. A. Bokuta, Elastic Constants and Elastic Moduli of Metals and Insulators Handbook, I. N. Frantsevich, Ed., Naukova Dumka: Kiev, Ukraine, 1983, pp. 60 – 180.

[33] V. Tvergaard, J. W. Hutchinson, J. Amer. Chem. Soc. 71 (1998) 157.

[34] P. Ravindran, L. Fast, P. A. Korzhavyi, B. Johansson, J. Wills, O. Eriksson, J. Appl. Phys. 84 (1998) 4891.

[35] D. H. Chung, W. R. Buessem, J. Appl. Phys. 38 (1967) 2010.

[36] S. I. Ranganathan, M. Ostoja-Starzewski, Phys. Rev. Lett. 101 (2008) 055504.

[37] C. M. Kube, AIP Adv. 6 (2016) 095209.

[38] Q. Wei, M. G. Zhang, L. X. Guo, H. Y. Yan, X. M. Zhu, Z. Z. Lin, P. Guo, Chem. Lett. 415 (2013) 36.

[39] O. L. Anderson, J. Phys. Chem. Solids 24 (1963) 909.

[40] E. Schreiber, O. L. Anderson, N. Soga, Elastic constants and their measurements, (McGraw-Hill, New York, 1973).

[41] C. Kittel, D. F. Holcomb, Am. J. Phys. 35 (1967) 547.

[42] D. R. Clarke, Surf. Coat. Technol. 163 (2003) 67.

[43] D. G. Cahill, S. K. Watson, R. O. Pohl, Phys. Rev. B 46 (1992) 6131.

[44] D. G. Cahill, R. O. Pohl, Annu. Phys. Chem. 39 (1988) 93.

[45] J. Callaway, Phys. Rev. 113 (1959) 1046.

Table 1. The present calculated structure parameters a, b, c (in Å) and cell volume (in Å^3) for MgB_2C_2 at 0 GPa compared with the experimental data [24] and previous theoretical results [25].

	a	b	c	V_0
This work	10.923	9.464	7.442	769.32
Experiment	10.922	9.461	7.459	770.83
Previous study	10.89	9.42	7.33	751.94

Table 2. The calculated coordinates of the eight atoms independent by symmetry in MgB_2C_2 at 0 GPa compared with the available experimental measurements [24] and the previous calculations [25].

	x			y			z		
Atom(site)	This work	Cal.	Exp.	This work	Cal.	Exp.	This work	Cal.	Exp.
Mg(8d)	0.1522	0.1532	0.1534	0	0	0	0	0	0
Mg(8f)	0	0	0	0.2787	0.2769	0.2798	-0.0104	-0.0110	-0.0113
B1(8e)	0.2500	0.2500	0.2500	0.0938	0.0934	0.0946	0.2500	0.2500	0.2500
B2(8f)	0	0	0	0.5883	0.5879	0.5886	0.2754	0.2741	0.2760
B3(16g)	0.1276	0.1275	0.1278	0.3406	0.3404	0.3415	0.2451	0.2433	0.2438
C1(8e)	0.2500	0.2500	0.2500	0.9265	0.9263	0.9271	0.2500	0.2500	0.2500
C2(8f)	0	0	0	-0.0795	-0.0797	-0.0792	0.2309	0.2342	0.2314
C3(16g)	0.1245	0.1245	0.1245	0.1744	0.1740	0.1750	0.2247	0.2239	0.2231

Table 3. Calculated elastic constants C_{ij} (in GPa) of MgB_2C_2 under different pressures.

Pressure	C_{11}	C_{12}	C_{13}	C_{22}	C_{23}	C_{33}	C_{44}	C_{55}	C_{66}
0	574.2	75.8	27.3	566.5	29.2	201.6	38.2	32.7	229.5
10	639.2	84.5	45.3	627.4	51.1	229.9	50.5	44.7	244.1
20	695.4	91.6	64.8	679.3	76.2	249.0	62.7	55.1	253.1
30	746.1	97.9	85.5	726.6	103.6	258.9	75.1	64.2	258.2
40	794.4	105.5	105.8	774.8	131.9	258.5	87.9	72.2	262.6
50	843.7	117.8	123.3	830.9	157.1	246.6	101.7	79.4	270.5

Table 4. The calculated density (ρ in g/cm^3), longitudinal, transverse and average sound velocities (V_L, V_T, V_M in m/s) and the Debye temperature (Θ_D in K) of MgB_2C_2 under different pressures.

Pressure	ρ	V_L	V_T	V_M	Θ_D
0	2.416	11.09	6.57	7.28	1019.2
10	2.577	11.59	6.86	7.59	1086.6
20	2.716	11.95	7.04	7.79	1135.3
30	2.843	12.20	7.14	7.92	1171.0
40	2.961	12.37	7.21	7.99	1197.8
50	3.075	12.45	7.24	8.04	1219.5

Table 5. The calculated acoustic velocities (v_l, v_{t1} and v_{t2} in m/s) in [100], [010], [001], [110], [101] and [011] directions of MgB_2C_2 under pressure up to 50 GPa.

	[100]			[010]			[001]		
Pressure	v_l	v_{t1}	v_{t2}	v_l	v_{t1}	v_{t2}	v_l	v_{t1}	v_{t2}
0	15.42	9.75	3.68	15.31	9.75	3.97	9.14	3.68	3.97
10	15.75	9.73	4.17	15.60	9.73	4.43	9.45	4.17	4.43
20	15.99	9.65	4.50	15.81	9.65	4.80	9.57	4.50	4.80
30	16.19	9.53	4.75	15.99	9.53	5.14	9.54	4.75	5.14
40	16.38	9.42	4.94	16.18	9.42	5.45	9.34	4.94	5.45
50	16.56	9.38	5.08	16.44	9.38	5.75	8.96	5.08	5.75
	[110]			[101]			[011]		
Pressure	v_l		$v_{t1}(v_{t2})$	v_l		$v_{t1}(v_{t2})$	v_l		$v_{t1}(v_{t2})$
0	3.83		12.87	7.44		9.33	7.37		9.35
10	4.30		13.05	7.56		9.64	7.49		9.64
20	4.66		13.16	7.62		9.85	7.54		9.85
30	4.95		13.22	7.66		9.98	7.53		9.99
40	5.20		13.29	7.69		10.05	7.52		10.10
50	5.43		13.42	7.78		10.08	7.54		10.20

Table 6. The calculated thermal conductivities ($k_{\min}$, k_l, k_{t1} and k_{t2} in $W{\cdot}m^{-1}{\cdot}K^{-1}$) in [100], [010], [001], [110], [101] and [011] directions of MgB_2C_2 under pressure up to 50 GPa.

	[100]				[010]				[001]			
Pressure	$k_{\min}$	k_l	k_{t1}	k_{t2}	$k_{\min}$	k_l	k_{t1}	k_{t2}	$k_{\min}$	k_l	k_{t1}	k_{t2}
0	2.068	1.105	0.699	0.264	2.082	1.098	0.699	0.285	1.204	0.655	0.264	0.285
10	2.349	1.248	0.771	0.330	2.359	1.237	0.771	0.351	1.429	0.749	0.330	0.351
20	2.579	1.368	0.825	0.385	2.589	1.352	0.825	0.411	1.615	0.819	0.385	0.411
30	2.771	1.473	0.866	0.432	2.787	1.453	0.866	0.467	1.767	0.867	0.432	0.467
40	2.941	1.567	0.901	0.472	2.970	1.548	0.901	0.522	1.888	0.894	0.472	0.522
50	3.078	1.640	0.943	0.494	3.109	1.619	0.943	0.546	1.976	0.936	0.494	0.546
	[110]				[101]				[011]			
Pressure	$k_{\min}$	k_l	k_{t1}	k_{t2}	$k_{\min}$	k_l	k_{t1}	k_{t2}	$k_{\min}$	k_l	k_{t1}	k_{t2}
0	2.119	0.275	0.923	0.923	1.871	0.534	0.669	0.669	1.869	0.528	0.670	0.670
10	2.409	0.341	1.034	1.034	2.128	0.599	0.764	0.764	2.122	0.593	0.764	0.764
20	2.648	0.398	1.125	1.126	2.337	0.652	0.843	0.842	2.328	0.644	0.842	0.842
30	2.855	0.449	1.202	1.202	2.511	0.696	0.907	0.907	2.502	0.684	0.908	0.908
40	3.043	0.498	1.272	1.272	2.660	0.736	0.962	0.962	2.653	0.719	0.967	0.967
50	3.184	0.521	1.331	1.331	2.784	0.771	1.007	1.007	2.777	0.753	1.012	1.012

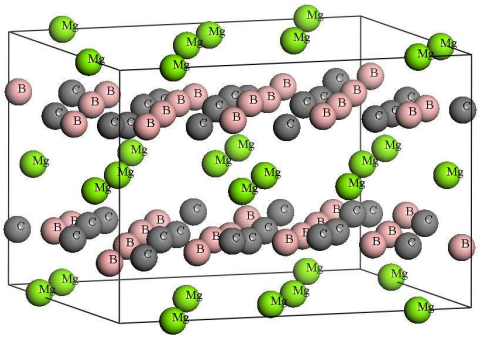

Figure 1: (Color online) Crystal structure of MgB_2C_2. Magnesium atoms are represented as green spheres, boron atoms as pink spheres, and carbon atoms as gray spheres.

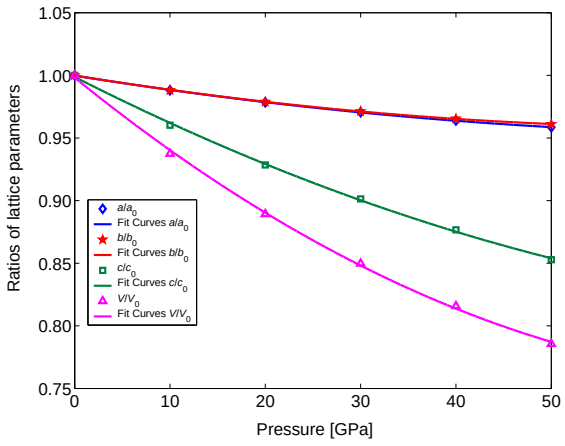

Figure 2: (Color online) The variations of structural parameters a/a_0, b/b_0, c/c_0 and cell volume V/V_0 of MgB_2C_2 with pressure range from 0 to 50 GPa. The discrete points and the solid lines denote the results from the first-principles calculations and the polynomial fitting, respectively.

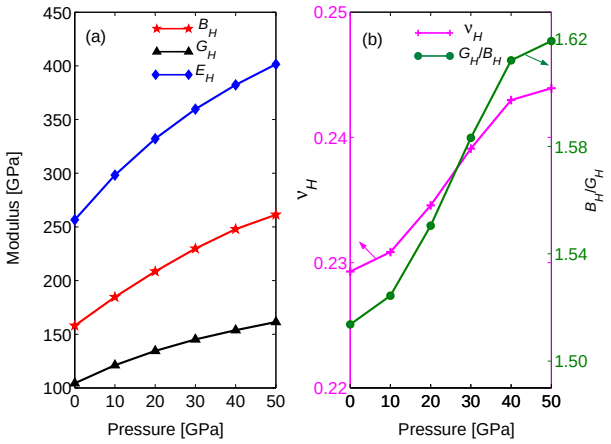

Figure 3: (Color online) Bulk (B_H), shear (G_H) and Young's (E_H) moduli (a) and Poisson's ratio ν_H and B_H/G_H ratio (b) as a function of pressure for MgB_2C_2.

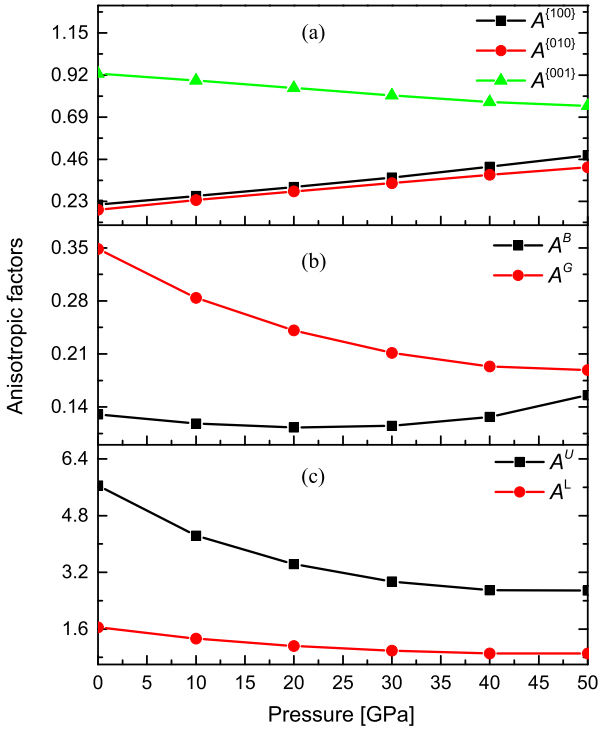

Figure 4: (Color online) Pressure dependence of various elastic anisotropies for MgB_2C_2: (a) the shear anisotropic factors $A^{\{100\}}$, $A^{\{010\}}$ and $A^{\{001\}}$, (b) the percentage anisotropy in compressibility A^B and shear A^G, (c) the universal elastic anisotropy A^U and the scalar log-Euclidean anisotropy A^L.

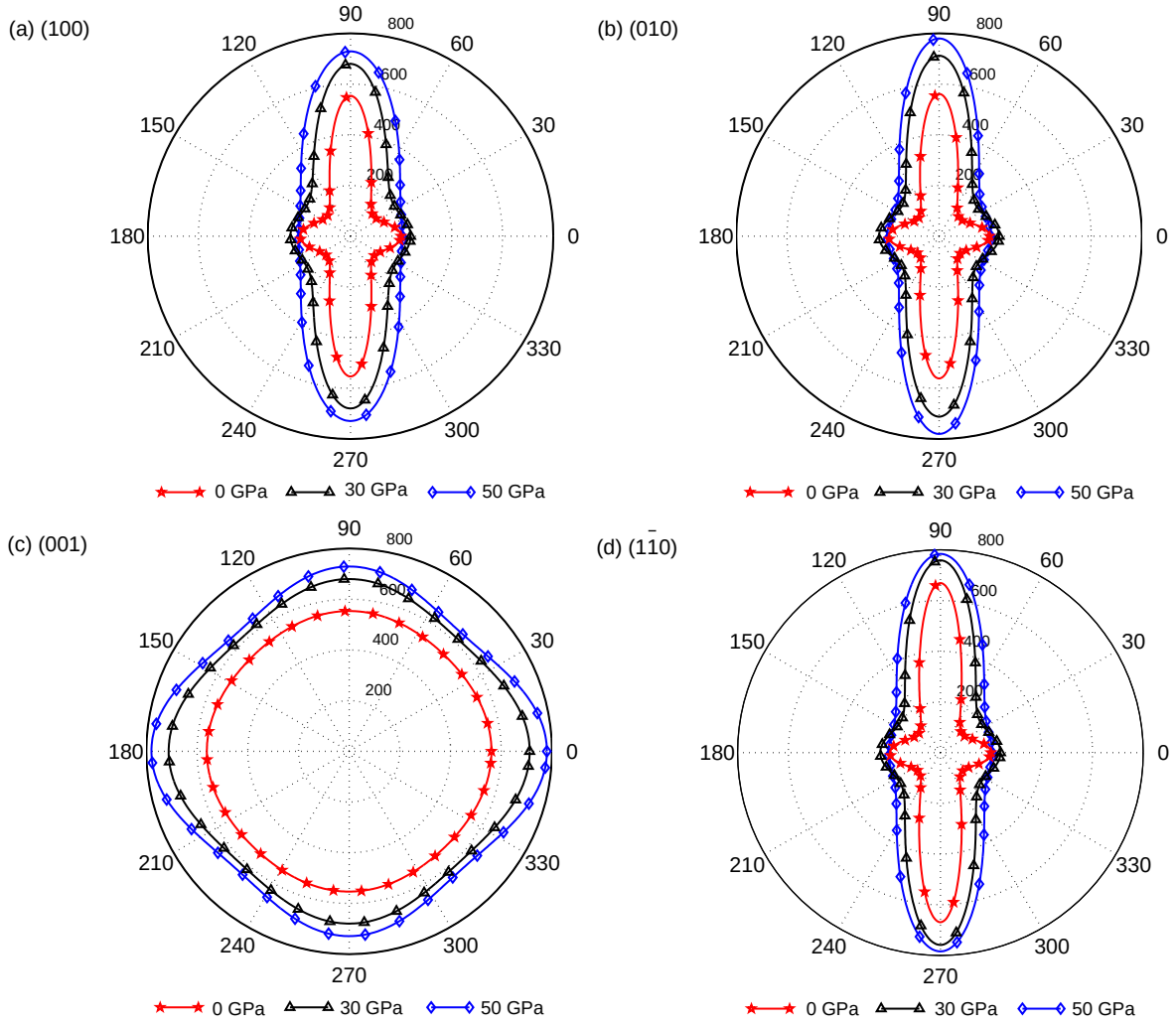

Figure 5: (Color online) The plane projections of the directional dependence of the Young's modulus in (100) (a), (010) (b), (001) (c) and (1$\bar{1}$0) (d) planes under different pressures.

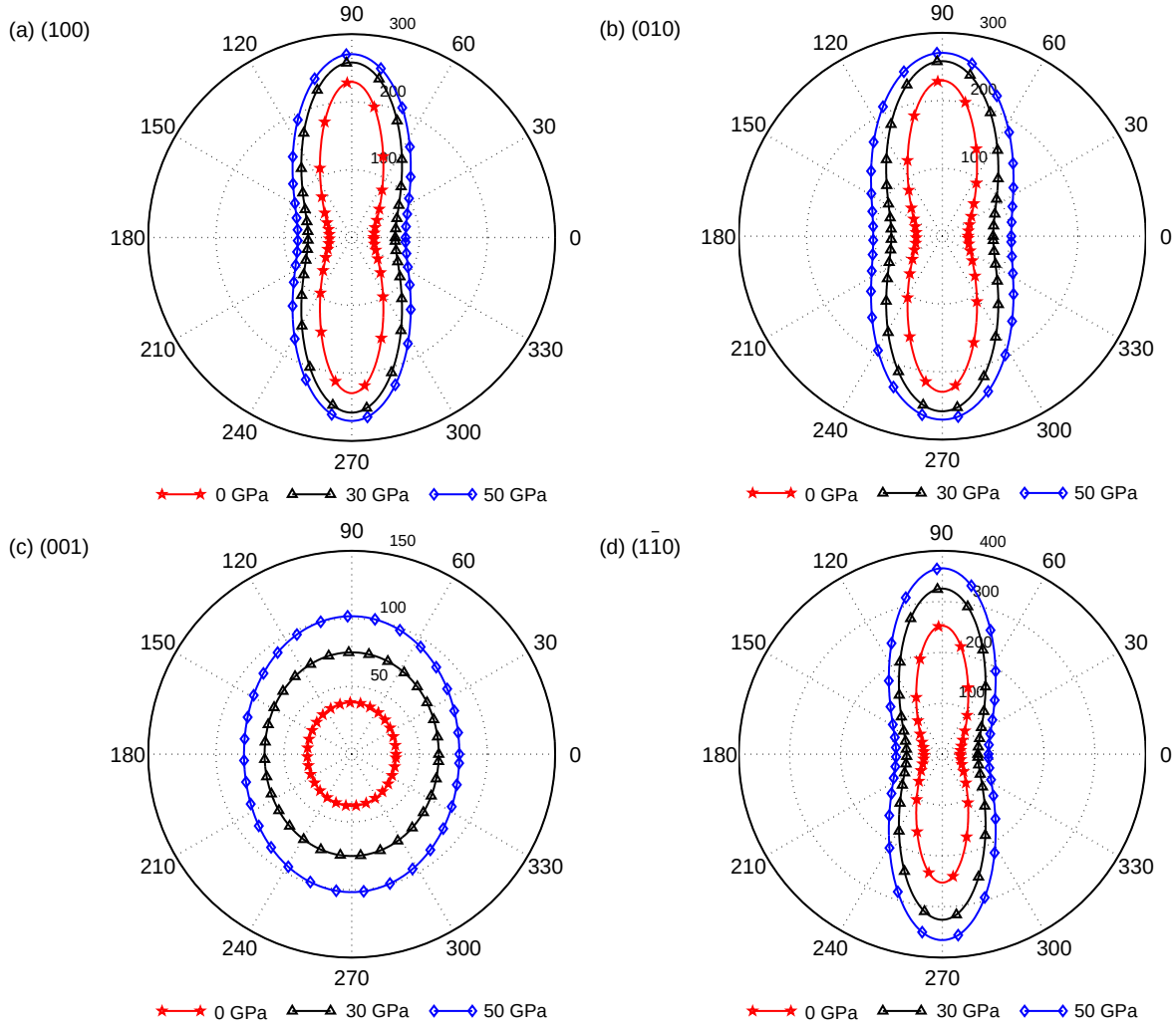

Figure 6: (Color online) The plane projections of the directional dependence of the shear modulus in (100) (a), (010) (b), (001) (c) and (1$\bar{1}$0) (d) planes under different pressures.

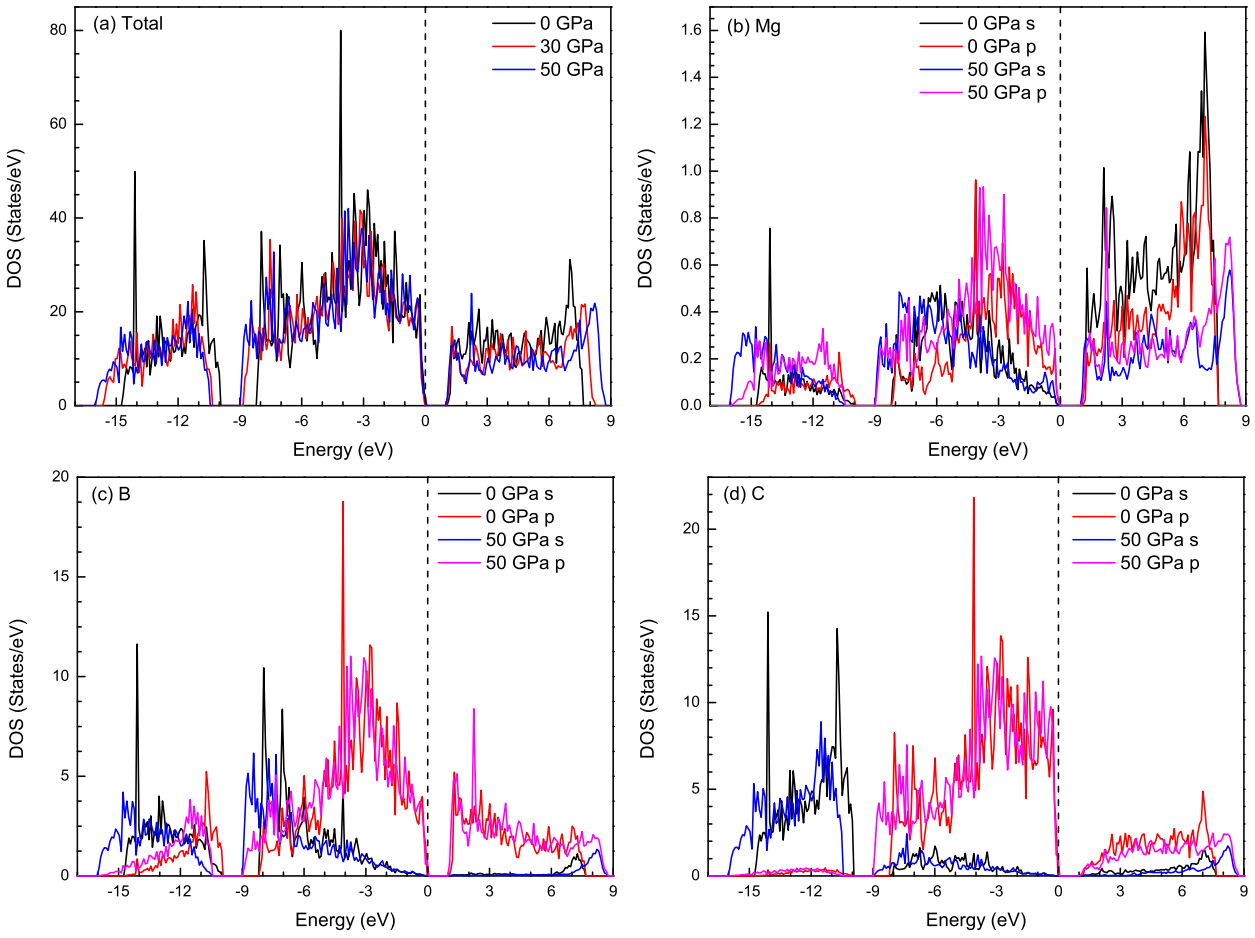

Figure 7: (Color online) Total and partial density of states of MgB_2C_2 under different pressures.